Chemical Science

ROYAL SOCIETY OF CHEMISTRY

EDGE ARTICLE

View Article Online
View Journal | View Issue

Cite this: *Chem. Sci.*, 2025, **16**, 16110

All publication charges for this article have been paid for by the Royal Society of Chemistry

Received 24th April 2025
Accepted 29th July 2025

DOI: 10.1039/d5sc03015c

rsc.li/chemical-science

Probing the influence of ion-pairing on ligand-field excited-state dynamics

Atanu Ghosh, Daniel Holmes and James K. McCusker *

Exploration of the photophysical and photochemical properties of transition metal complexes has driven ground-breaking advancements in solar energy conversion technologies, including photoredox catalysis. While significant research has been devoted to understanding excited state properties of second- and third-row transition metal complexes, earth-abundant first-row metal complexes have received comparatively little attention in this context until very recently. In particular, the role of ion-pairing – which has been identified as a potentially significant factor for Ir(III)-based photosensitizers – has not been examined with regard to its influence on the ligand-field excited states that dominate much of first-row photophysics. A key challenge in studying ion-pair interactions lies in quantifying the extent and nature of ion-pairing, particularly in non-aqueous media where the vast majority of photophysical studies are performed. Cobalt(III) polypyridyl complexes provide an attractive platform to address such questions due to their demonstrated potential for applications in photoredox catalysis involving ligand-field excited states. In the present study, we prepared a cobalt(III) polypyridyl complex, $[Co(4,4'\text{-}OMebpy)_3](BAr^F{}_4)_3$ (where 4,4′-OMebpy is 4,4′-dimethoxy-2,2′-bipyridine and $BAr^F{}_4$ is tetrakis(3,5-bis(trifluoromethyl)-phenyl)borate) to probe ion-pairing in non-aqueous solutions. Specifically, analysis of data acquired from both variable-temperature diffusion ordered spectroscopy (DOSY) NMR and 1-D rotating-frame nuclear Overhauser effect (ROE) experiments allowed us to identify and differentiate between solvent-separated ion pairs in high-dielectric media and contact ion pairs in a low-dielectric solvent. Time-resolved absorption spectroscopy was then used to measure ground-state recovery dynamics under these varying conditions of ion-pairing, the results of which revealed an increase in excited-state lifetime for contact ion-pairs that we suggest arises from a reduction in outer-sphere reorganization energy relative to conditions which favored solvent-separated ion pairs. We believe this study demonstrates that one can leverage broadly available NMR-based methods to understand ion-pairing in non-aqueous solutions, which in turn can provide a microscopic picture of intermolecular interactions that can impact the photophysical properties of transition metal-based chromophores.

Introduction

Photoredox catalysis using transition metal complexes has become a vibrant and expanding field in chemistry.[1–6] A key advantage of these transition metal complexes is the versatility of the metal center, which can exhibit multiple redox states, adopt various coordination geometries, and possess tunable absorption cross-sections in the visible region of the spectrum. These properties make transition metal complexes highly versatile for many photoredox applications, particularly in the context of organic transformations where optical differentiation between the photocatalyst and substrate is a critically important design criterion. Since most metal complexes are charged, they require a counterion for charge balance, the choice of which directly impacts the compound's solubility. While this provides a facile mechanism for potentially utilizing a given photocatalyst in a wide range of solvents, changes to the identity of the counterion coupled with variations in the dielectric constant of the solvent will invariably lead to differences in the degree of ion aggregation in a given reaction medium. The existence of ion-paired photoredox catalysts has been documented,[7–10] but what is less known/investigated is the extent to which these coulombic interactions impact the photophysical properties of the chromophores, *e.g.*, excited-state lifetimes and energetics.[11–13] Understanding ion-pair structures in this context is therefore crucial, since the properties just enumerated have a profound influence on the compound's photofunctionality.[11–13] Ion-pairs are generally classified into three broad categories:[14,15] (a) solvent-separated, (b) solvent-shared, and (c) contact ion-pairs, all three of which are schematically shown in Fig. 1.

Although ion-pairing has been exploited in organic chemistry, it has not been examined extensively in the context of inorganic

Department of Chemistry, Michigan State University, East Lansing, USA. E-mail: jkm@chemistry.msu.edu

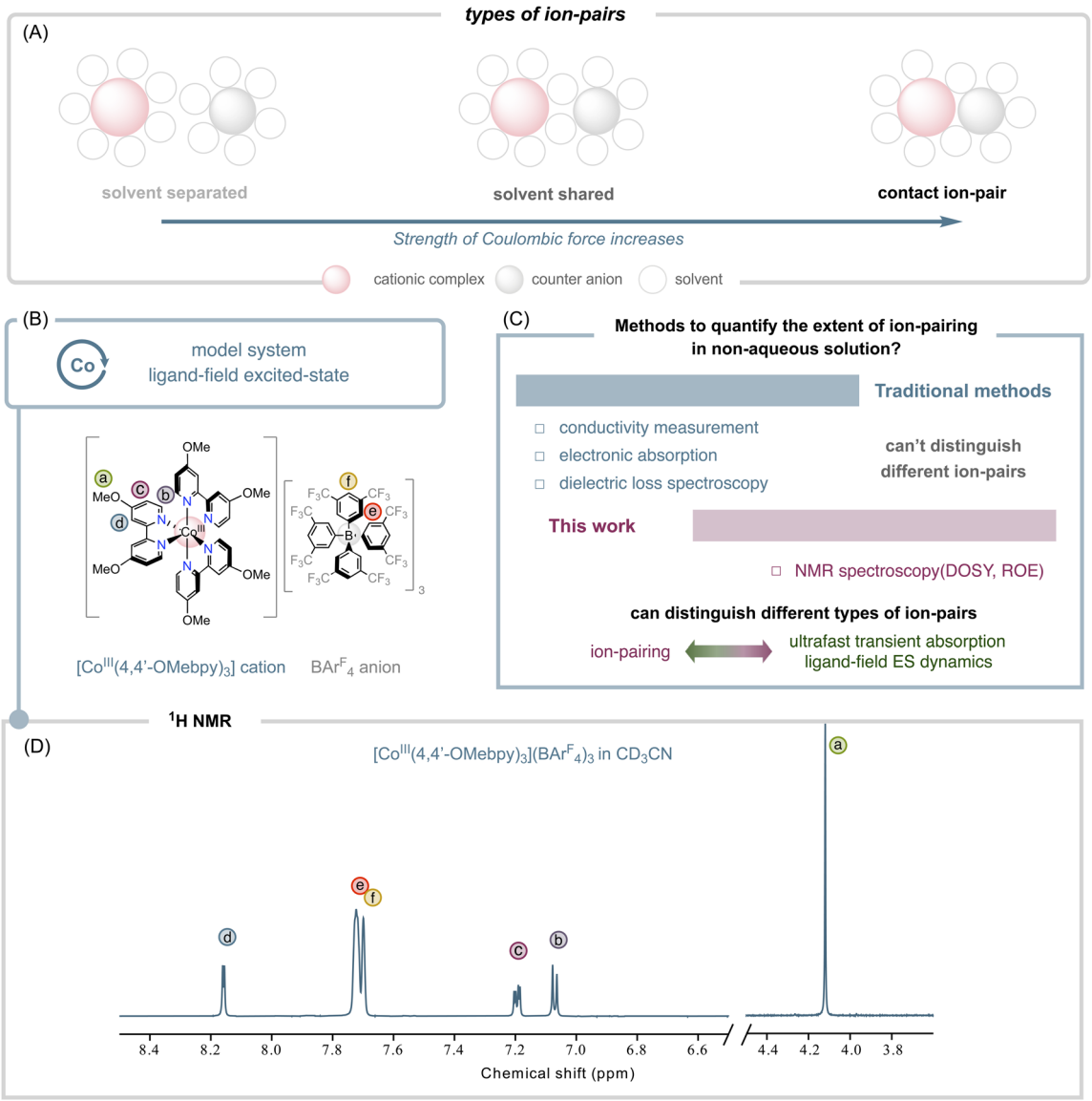

Fig. 1 (A) Schematic representation of different types of ion-pairs in solution with increasing coulombic interaction between the ions from left to right. (B) Drawing of the complex [Co(4,4′-OMebpy)$_3$](BAr^F)$_3$ used in this study. (C) Various methods used to probe ion-pairing, including the NMR methods described in this work wherein the ion-pairing analysis will be coupled with time-resolved absorption measurements to assess any correlation between ion-pairing and excited-state lifetime. (D) ^{1}H NMR spectrum of [Co(4,4′-OMebpy)$_3$](BAr^F)$_3$ acquired in CD_3CN solution, along with assignments.

photochemistry primarily due to challenges associated with the characterization of ion-pairing in non-aqueous solutions where most photoredox studies are performed.[7,8,16–18] Conductivity measurement is arguably the most established method of analysis to quantify ion-pairing[14,19] for 1 : 1 ion pairs in aqueous solution but remains challenging for higher-order ion pairs.[14] Additionally, this method is susceptible to trace amounts of water, significantly limiting its reliability and/or reproducibility in non-aqueous solutions. Another common method for quantifying ion-pairing interactions involves titrating one ion into a solution of the other ion and observing changes in physical properties using UV/vis absorption, emission, nuclear magnetic resonance (NMR), or other spectroscopic techniques.[14,20–22] Such methods have been used to understand the effects of ion-pairing on the excited-state properties of charge-transfer based chromophores, such as ruthenium(II) and iridium(III) based chromophores.[20,23–28] These studies indicate that ion-pairing interactions can alter excited state dynamics, cage escape yields, and excited state quenching mechanisms, thereby influencing product selectivity in photoredox catalysis.[10,11,17,29–34] Time-resolved dielectric-loss (TRDL) spectroscopy has recently been employed to gain insights into the ground- and excited-state ion-pairing in a iridium(III) based photosensitizer.[17] This method, which relies on measuring a large dipole moment to quantify ion-pairing, holds tremendous promise but requires specialized equipment and training and is therefore somewhat limited in terms of broad applicability at the present time. Moreover, TRDL experiments are best carried out in low dielectric solvents and may be less effective for studying

higher-order ion pairs due to the symmetric arrangements of the counterions which often reduces the effective intermolecular dipole moment to which the measurement is sensitive.

As mentioned above, the influence of ion-pairing on charge-transfer excited state dynamics has been studied previously,[20,28] but corresponding studies involving ligand-field excited states have not been reported.[35] Given the increasing awareness of the potential of this class of excited states for effecting organic transformations[5,36–43] coupled with the fact that the compounds that have been employed in this context are typically highly charged (*i.e.*, >+1), we sought to assess to what extent ion-pairing influences the photophysical properties of ligand-field excited states. Cobalt(III) polypyridine complexes, whose photophysical properties we have recently described,[44] present an excellent opportunity to explore such effects. With this contribution we therefore sought to quantify the degree of ion-pairing present in different non-aqueous solutions of a cobalt(III) polypyridyl complex, $[Co(4,4'\text{-OMebpy})_3](BAr^F{}_4)_3$ (where 4,4′-OMebpy is 4,4′-dimethoxy-2,2′-bipyridine and $BAr^F{}_4$ is tetrakis(3,5-bis(trifluoromethyl)-phenyl)borate) using widely available NMR-based methods. Specifically, we carried out diffusion-ordered spectroscopy (DOSY) and variable-temperature (VT) DOSY measurements in a series of non-aqueous solvents, which allowed us to both quantify the degree of ion-pairing present in solution as well as differentiate between solvent-separated and contact ion-pairs under various conditions. Additionally, 1-D rotating-frame nuclear Overhauser effect (ROE) experiments provided additional insights into the through-space interactions between the ions, which in turn provided information about the relative spatial orientation of the counter anions with respect to the cobalt(III) cation. Time-resolved electronic absorption spectroscopy was then employed to assess the influence of the different types of ion-pairing identified from the NMR experiments on the excited-state lifetime of the Co(III) complex. The results reveal that this approach represents a viable and easily accessible method for characterizing ion-pairs in solution and correlating the existence and nature of those ion pairs to the dynamics of ligand-field excited states.

Experimental methods

Materials

$Co(BF_4)_2 \cdot 6H_2O$ was purchased from Oakwood chemicals, 4,4′-dimethoxy-2,2′-bipyridine, DDQ were purchased from Ambeed and Sigma respectively. $NaBAr^F{}_4$ was donated by Kelly Aldrich. For NMR studies all deuterated solvents were purchased from Cambridge Isotope Laboratories Inc. and used without further purification. Spectroscopic grade solvents were purchased from the following resources and used for ligand-field studies and transient absorption kinetic measurements: acetonitrile (Sigma-Aldrich, 34851), acetone (Fisher chemical, A949-1), dichloromethane (Jade Scientific, JS-D2735), and nitromethane (Sigma-Aldrich, 270423).

DOSY and 1D ROE NMR methods

All NMR experiments were run on a Bruker Avance III HD 500 MHz NMR spectrometer equipped with a 5 mm BBFO NMR probe. DOSY NMR experiments were run using the dstebpgp3s pulse program (double stimulated echo for convection compensation and LED using bipolar gradient pulses). Gradient duration and diffusion delays were determined for each sample and temperature such that the signal intensities at maximum gradient strength were between 10–20% of the intensities at lowest gradient setting, ROE measurements were run using the selrogp pulse sequence. All data were processed using MestreNova software. For variable temperature DOSY measurements, temperature control was achieved using a BCU-II cooling unit and temperatures were calibrated with either pure methanol or 80% ethylene glycol in DMSO-d_6.

Electronic absorption spectroscopy

Electronic absorption spectra were collected using a double-beam PerkinElmer Lambda 1050 spectrophotometer. Spin-allowed ligand-field transitions were measured in 1 cm pathlength quartz cells, whereas spin-forbidden ligand-field transitions were measured in a 10 cm pathlength quartz cell; for the latter a manual subtraction of the solvent blank was performed as described in our earlier report.[45] Gaussian deconvolution was performed to accurately determine transition energies and molar absorptivities associated with the transitions, the procedure for which is described in the SI file.

Transient absorption spectroscopy

Time-resolved electronic absorption data were acquired using a home-built laser system that has been described previously.[46] The instrument response function (IRF) was determined to be ~150 fs based on a measurement of the optical Kerr effect in methanol, fitting the signal to a Gaussian, and extracting the FWHM using Igor Pro software. Samples were prepared by dissolving the complex in the respective solvents such that the absorbance at the pump wavelength (480 nm) was between 0.4–0.6 OD. These conditions also ensured that the concentration used for both the NMR and TA experiments were comparable so that the desired correlations could be meaningfully assessed.

Density functional theory calculations

All calculations were carried out using Gaussian 16 revision C.001 (ref. 47) software package available through High Performance Computing Centre (HPCC) of the Institute for Cyber-Enabled Research (ICER) at Michigan State University. Methods to compute transition energies have been discussed elsewhere,[44] but in short, geometry optimization of singlet and triplet ground states were performed using density functional theory (DFT) level of theory, followed frequency calculations to confirm local minima. For simplicity, counter anions were not included in the calculations. A conductor-like polarizable continuum model (CPCM) was employed for all solvents. B3LYP+D2 functional and the def2-TZVP basis (for Co) and 6-311G++(d) (all other atoms) were used for geometry optimization and frequency calculations, whereas single-point energy calculations were calculated at the B3LYP+D2/6-311G++(d,p) level of theory. No symmetry criteria were imposed for any of the calculations.

Results and discussion

Design strategy for the cobalt(III) model complex

For probing ion-pairing using DOSY NMR, 4,4′-dimethoxy-substituted 2,2′-bipyridine ligand was chosen as the basis for the cobalt(III) complex, $[Co(4,4'\text{-OMebpy})_3](BAr^F{}_4)_3$ for two primary reasons: (1) the desire to have both the Co(III) cation and $BAr^F{}_4$ counter-anion possess distinct ^{1}H NMR signals, which will facilitate the DOSY NMR interpretation as only ^{1}H DOSY would be needed, and (2) the fact that the π-donating nature of the methoxy substituents increases the excited state absorption signal by stabilizing the higher energy ligand-to-metal charge-transfer excited-state(s), which in turn leads to a significant increase in the signal-to-noise ratio of the time-resolved absorption data acquired in the visible region probe window (400–720 nm). The model complex was synthesized following previously reported procedure,[48] The compound was characterized by ^{1}H, ^{19}F NMR, and ESI-MS, the details of which can be found in the SI. The ^{1}H NMR spectrum of the complex (in CD_3CN) is shown in Fig. 1, which includes the assignments of all of the peaks and demonstrates that both the ions have easily distinguishable ^{1}H NMR resonances.

Diffusion ordered spectroscopy (DOSY)

DOSY NMR has been routinely employed to study weak interactions in solution.[49–52] This method relies on the well-established relationship between the diffusion coefficient and molecular size, which can be approximated by the Stokes–Einstein equation,

$$D = \frac{kT}{6\pi\eta r_H} \quad (1)$$

where D is the diffusion constant, k is the Boltzmann constant, T is the temperature, η is the viscosity of the solvent, and r_H is the hydrodynamic radius of the species in question. In the case of ion-pairing, the hydrodynamic radius can indirectly reflect the strength of ion-pairing interaction, as stronger interactions will create a larger "effective" entity, *i.e.*, the associated Co(III) complex and counterion, which will manifest as a smaller diffusion constant.

As the coulombic force between two opposite charges can be tuned by changing the dielectric medium, ^{1}H DOSY NMR experiments were conducted in four different solvents covering a broad range of static dielectric constants (ε): CD_2Cl_2 (8.93), acetone-d_6 (21.01), CD_3CN (36.64) and CD_3NO_2 (37.27). Furthermore, using CD_3CN and CD_3NO_2, which have comparable dielectric constants, enables us to assess whether the dielectric constant is the primary contributing factor in modulating ion-pairing strength or if other factors (*e.g.*, the presence of trace amount of water, solvent donor strength, *etc.*) play a significant role. The ^{1}H DOSY spectra of $[Co(4,4'\text{-OMebpy})_3](BAr^F{}_4)_3$ in CD_3CN and CD_2Cl_2 under identical conditions of concentration, volume, and temperature are shown in Fig. 2A and B, respectively; analogous ^{1}H DOSY spectra of the complex in acetone-d_6 and CD_3NO_2 are provided in the SI. The diffusion constants are plotted as a function of chemical shifts. Resonances originating from a single species are expected to have the same diffusion constant. In contrast, associated species in solution would give rise to a different diffusion coefficient depending on the strength of the interaction. Diffusion constants for both ions in all four solvents are summarized in Table 1.

The DOSY data reveal significantly higher diffusion constants for $[BAr^F{}_4]^-$ anion (Table 1, entry 2) as compared to $[Co(4,4'\text{-OMebpy})_3]^{3+}$ (Table 1, entry 1) in all four solvents. These differences can be explained quite readily by the Stokes–Einstein equation (eqn (1)). Put simply, this equation indicates that species with smaller hydrodynamic radii (*e.g.* $[BAr^F{}_4]^-$ in this case) will have higher diffusion constant than those with larger hydrodynamic radii (*e.g.*, $[Co(4,4'\text{-OMebpy})_3]^{3+}$). Furthermore, the diffusion constant is inversely proportional to the solvent

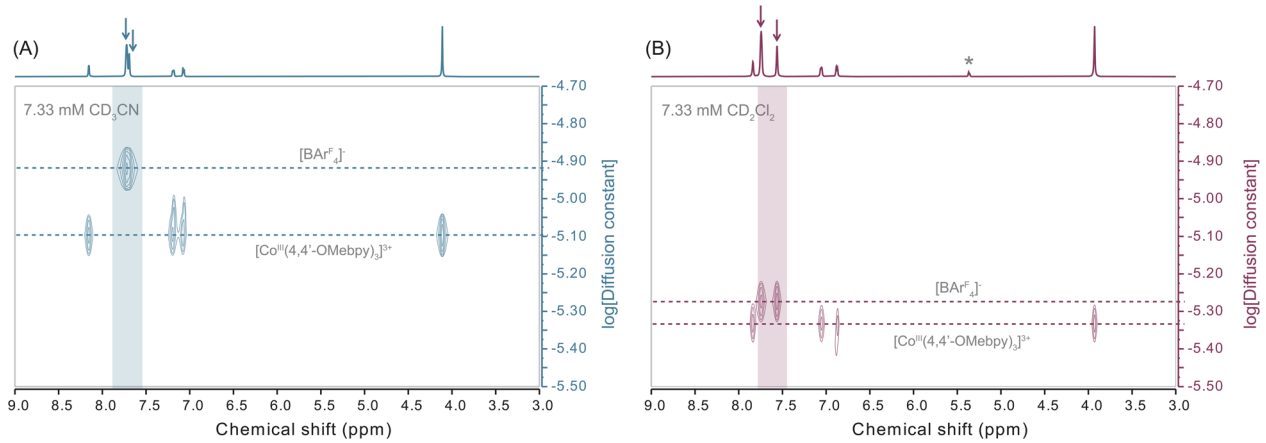

Fig. 2 ^{1}H DOSY NMR spectrum of $[Co(4,4'\text{-OMebpy})_3](BAr^F{}_4)_3$ complex in CD_3CN (A) and CD_2Cl_2 (B), collected under identical conditions of concentration (7.33 mM), volume (600 μL), and temperature (25 °C). For clarity, only the chemical shift region characteristic of the complex under investigation is shown; the dotted lines on the plots are provided to guide the eye regarding the diffusion constant. The arrows represent the ^{1}H signals originating from the $BAr^F{}_4$ counter anion in the two solvents. The asterisk on the NMR spectrum shown in panel B represents a solvent peak. The relative gaps between the dotted lines can be directly correlated to the extent of ion-pairing in solution: see text for further details.

Table 1 Diffusion constant and viscosity-weighted diffusion constants for $[Co(4,4'\text{-OMebpy})_3]^{3+}$ and $[BAr^F{}_4]^-$ ions in CD_3NO_2, CD_3CN, acetone-d_6 and CD_2Cl_2 obtained from DOSY NMR experiments performed at 25 °C. Solvents viscosities and static dielectric constants for the respective non-deuterated solvents are also provided

Solvents			CD_3NO_2	CD_3CN	Acetone-d_6	CD_2Cl_2
Viscosity (mPa s)			0.630	0.369	0.306	0.413
Static dielectric constant			37.27	36.64	21.01	8.93
D (10^{-6} cm^2 s^{-1})	1	$[Co(4,4'\text{-OMebpy})_3]^{3+}$	3.90 ± 0.20	6.40 ± 0.20	6.10 ± 0.20	3.37 ± 0.20
	2	$[BAr^F{}_4]^-$	5.25 ± 0.20	9.02 ± 0.20	9.00 ± 0.20	4.10 ± 0.20
$D \times \eta$ (10^{-6} cm^2 mPa)	3	$[Co(4,4'\text{-OMebpy})_3]^{3+}$	2.40 ± 0.12	2.36 ± 0.07	1.87 ± 0.06	1.40 ± 0.08
	4	$[BAr^F{}_4]^-$	3.28 ± 0.13	3.33 ± 0.07	2.75 ± 0.06	1.69 ± 0.08

viscosity, which means that at a constant temperature, if the hydrodynamic radii of a species remain unchanged across all solvents, the diffusion coefficient should decrease as viscosity increases. The DOSY data from our measurements clearly do not align with this latter expectation: the smallest diffusion constants for both ions were observed in CD_2Cl_2, rather than in CD_3NO_2, which is the most viscous solvent among the four, indicating the hydrodynamic radii of the ions across all solvents must be different.

As mentioned previously, while hydrodynamic radii can be viewed as a reporter for the strength of ion-pairing in solution, the interdependence between diffusion constants and solvent viscosity complicates the task of establishing a direct correlation between the dielectric constant of the solvent and the ion-pairing strength. To address this, we factored in the effect of viscosity into the diffusion constants by considering their product (*i.e.*, $D \times \eta$, Table 1, entry 3 and 4). With this recasting of the data, the viscosity-weighted diffusion constant ($D \times \eta$) for $[Co(4,4'\text{-OMebpy})_3]^{3+}$ (Table 1, entry 3) decreases systematically from (2.40 ± 0.12) × 10^{-6} cm^2 mPa in CD_3NO_2 to (1.40 ± 0.08) × 10^{-6} cm^2 mPa (CD_2Cl_2), *i.e.*, it now tracks with the dielectric constant of the solvent. A similar trend is observed for $[BAr^F{}_4]^-$ counterions (Table 1, entry 4), with the highest values observed in the solvents with the highest dielectric constants (CD_3NO_2 and CD_3CN). We interpret these trends – which directly reflect changes in hydrodynamic radii – as an indicator of variations in the extent of ion-pairing, with the dielectric constant of the solvent emerging as a critical factor in controlling ion-pairing in solution. Specifically, the significant decrease in the $D \times \eta$ term for both ions on going from CD_3CN (dielectric constant of 36.64) to CD_2Cl_2 (dielectric constant of 8.93) implies that the strength of ion-pairing interaction is greater in the lower dielectric solvent, which leads to a larger effective hydrodynamic radius and a systematic decrease in the diffusion constants across the solvent series. This observation also aligns with the larger relative differences in the diffusion constants of $[Co(4,4'\text{-OMebpy})_3]^{3+}$ and $[BAr^F{}_4]^-$ in CD_3CN (~2.62 cm^2 s^{-1}) as compared to CD_2Cl_2 (~0.73 cm^2 s^{-1}) (Fig. 2).

To investigate broader applicability of this method of probing ion-pairing in solution – as well as examine a system that might be expected to exhibit an even greater degree of ion pairing – we also performed analogous ^{1}H DOSY and ^{19}F DOSY measurements on $[Co(4,4'\text{-OMebpy})_3](PF_6)_3$. The data and analysis from these studies – which are provided in the SI – yielded similar results to those we obtained for the $[BAr^F{}_4]^-$ salt. Since the latter exhibits solubility in a broader range of solvents, we will focus primarily on data acquired on $[Co(4,4'\text{-OMebpy})_3](BAr^F{}_4)_3$ for the remainder of the discussion.

Variable-temperature (VT) DOSY studies

The ^{1}H DOSY data just presented provides insights into the extent of ion-pairing but does not reveal details about the specific nature of the ion pairs, *i.e.*, contact ion pairs *versus* solvent-separated. To examine this issue, we carried out variable-temperature DOSY experiments. The VT ^{1}H DOSY experiments were conducted in the same solvents over a temperature range of 268 K to 298 K, in 5 K increments. The viscosity-weighted diffusion constants of the ions are plotted against the absolute temperature in Fig. 3, using our modified Stokes–Einstein equation (eqn (2)), to linearize the data and allow us to determine the hydrodynamic radii (r_H) of the diffusing species in different solvents.

$$D\eta = \frac{kT}{6\pi r_H} \tag{2}$$

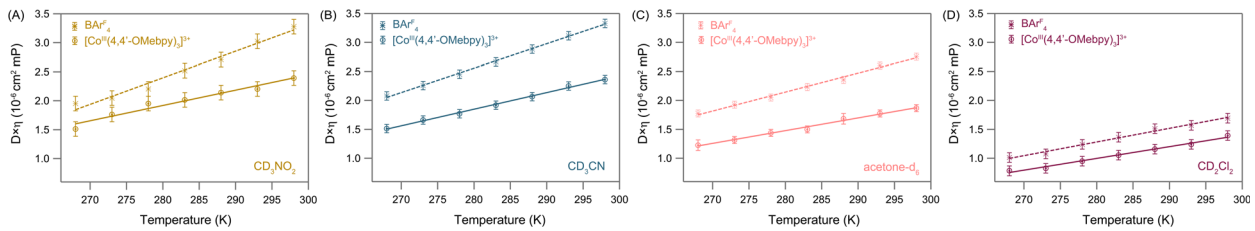

Fig. 3 Variable-temperature DOSY NMR data for $[Co(4,4'\text{-OMebpy})_3](BAr^F{}_4)_3$ in CD_3NO_2 (A), CD_3CN (B), acetone-d_6 (C), and CD_2Cl_2 (D). The viscosity-weighted diffusion constant ($D \times \eta$) of both the cation and anion are each plotted as a function of temperature. The lines represent fits of the data for $[Co(4,4'\text{-OMebpy})_3]^{3+}$ (solid) and $[BAr^F{}_4]^-$ (dashed) to eqn (2). See text for further details.

Quantitatively accounting for the temperature dependence of solvent viscosity is a challenging problem as it is highly model-dependent.[53] For the purposes of this discussion, room temperature (25 °C) viscosity values were used for the viscosity weighting of the diffusion constant presented in Fig. 3; analyses in which viscosity adjustments for temperature using several simplified models yielded qualitatively similar results and are detailed in the SI. It is evident from the data that for all ions, the $D \times \eta$ values increase with increasing temperature, consistent with eqn (2). As expected given their difference in size and overall charge, $D \times \eta$ is larger for the $[BAr^F{}_4]^-$ anion as compared to $[Co(4,4'\text{-OMebpy})_3]^{3+}$ at all temperatures. For both ions, we note that the slope of the $D \times \eta$ *vs.* T plot systematically decreases with decreasing dielectric constant of the solvent: based on eqn (2), this implies an increase in the effective hydrodynamic radii for both ions, an observation we attribute to an increase in the degree of ion-pairing as the dielectric constant of the solvent is reduced. Interestingly, the slope from the linear fit for the $[BAr^F{}_4]^-$ anion in CD_3NO_2, CD_3CN and acetone-d_6 is larger than that of the cation, giving rise to a divergence between the viscosity-weighted diffusion constants for the two ions with increasing temperature. As the slope of the plot is inversely proportional to the hydrodynamic radii, the data indicate that the effective hydrodynamic radius of $[BAr^F{}_4]^-$ is smaller in comparison to the cationic counterpart. The ability to differentiate the sizes of the two ions in this manner suggests a physical picture consistent with solvent-separated ion-pairing under these conditions. In contrast, the slopes of the $D \times \eta$ *vs.* T plots in CD_2Cl_2 for both the ions are similar, giving rise to two parallel fit lines as opposed to the divergent lines in the other three solvents (Fig. 3D). These observations indicate that the hydrodynamic radii for both the ions are effectively the same: by similar reasoning, we suggest this observation as being strongly indicative of contact ion-pairing wherein the ions diffuse as a single entity fostered by the low dielectric constant associated with CD_2Cl_2.

An alternative, perhaps more intuitive way of interpreting the VT data is by considering the available thermal energy balanced against the magnitude of the dissociation energy associated with the contact ion-pair. Ion-pairing structures in solution can be viewed as an equilibrium between contact and solvent separated ion-pairs as shown in eqn (3):

$$\left\{\left[Co(4,4'\text{-OMebpy})_3\right]^{3+}\right\}\cdot\left[BAr^F{}_4\right]^- \overset{+S}{\rightleftharpoons} \left\{\left[Co(4,4'\text{-OMebpy})_3\right]^{3+}\cdot S\cdot\left[BAr^F{}_4\right]^-\right\} \quad (3)$$

Overcoming the coulombic attraction giving rise to the contact ion-pair is an endothermic process but should be entropically favored: provided the overall free energy is on the order of k_BT, the fraction of solvent separated ion-pairs should increase with increasing temperature. We believe this is the most likely origin for divergent nature of the $D \times \eta$ *vs.* T plots in CD_3NO_2, CD_3CN and acetone-d_6, *i.e.*, thermal energy coupled with the stronger solvating ability of the higher dielectric solvents is sufficient in this temperature range to shift the equilibrium expressed in eqn (3) to the right, *i.e.*, toward the solvent-separated pairs. Qualitatively, we note that the degree of divergence is inversely tracking the dielectric constant of these solvents, *i.e.*, the slopes exhibit their largest discrepancy in CD_3NO_2, slightly smaller in CD_3CN, and considerably less so in acetone-d_6. In contrast, we do not observe any such divergence in the $D \times \eta$ *vs.* T plot for CD_2Cl_2, *i.e.*, the two ions are moving together over the entire temperature range sampled. We submit that this is due to the lower dielectric constant of this solvent and a corresponding inability to overcome the coulombic attraction associated with the contact ion pair.

1-D ROE measurements

To further examine the nature of the ion-pairing interaction, we conduced 1-D ROE NMR experiments in CD_3CN and CD_2Cl_2. Briefly, for these experiments, a frequency-selective pulse inverts the spin population of the methoxy protons, resulting in inverted proton signals. Protons within 5–7 Å of these inverted spins display a small positive enhancement, resulting in a positive signal, while protons beyond 7 Å have negligible enhancements and are typically not detected. The 1-D ROE data for $[Co(4,4'\text{-OMebpy})_3](BAr^F{}_4)_3$ in CD_3CN and CD_2Cl_2 are shown in Fig. 4. In CD_3CN the 1-D ROE data reveals three positive peaks, corresponding to intramolecular interactions within the 4,4′-dimethoxy-2,2′-bipyridine ligand (Fig. 4, left panel). The absence of additional signals from $[BAr^F{}_4]^-$ suggests no through-space coupling between the $[Co(4,4'\text{-OMebpy})_3]^{3+}$ and $[BAr^F{}_4]^-$ within 7 Å, consistent with the solvent separated ion-pair assignment we derived from the DOSY NMR experiments. In contrast, 1-D ROE measurements in CD_2Cl_2 reveal two additional positive ROE signals along with three intramolecular interactions within the 4,4′-dimethoxy-2,2′-bipyridine ligands, which corresponds to the $[BAr^F{}_4]^-$ counterion (Fig. 4, right panel). This result indicates strong contact ion-pair interaction between the cation and the anion, with a maximum space separation of approximately 5–7 Å. To further investigate the ion-pair structures, we performed additional 1-D ROE experiments in CD_2Cl_2 – described in greater detail in the SI – in which the ROE intensity on the proton signals of $[BAr^F{}_4]^-$ were monitored by inverting the $[Co(4,4'\text{-OMebpy})_3]^{3+}$ protons. It was found that the maximum ROE signal was observed when the 5,5′-protons of the bipyridine were inverted, strongly suggesting that the $[BAr^F{}_4]^-$ counter ions are located in the space between the substituted bipyridine ligands in the primary coordination sphere of the metal. A space-filling model depicting this proposed contact ion-pair configuration is provided in Fig. S14.

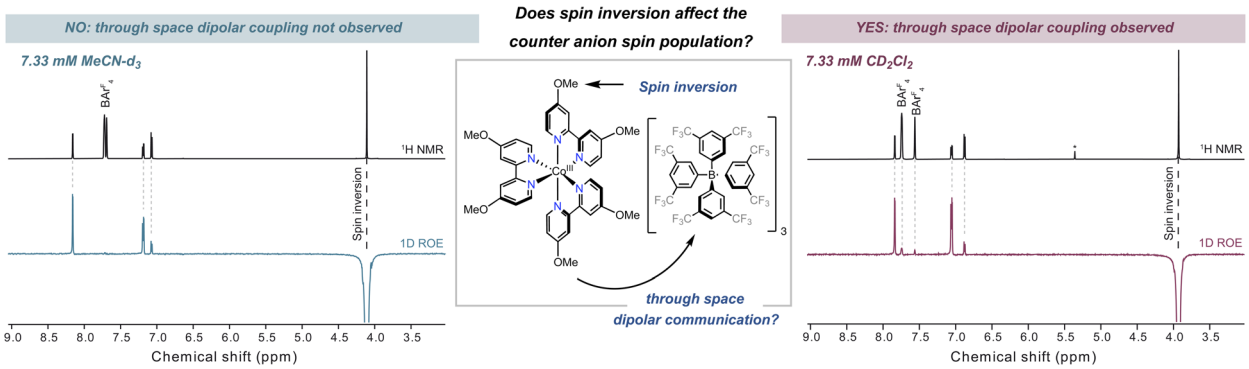

Fig. 4 $^{1}H-^{1}H$ 1D-Rotating frame nuclear Overhauser effect (ROE) data for $[Co(4,4'\text{-}OMebpy)_3](BAr^F{}_4)_3$ in CD_3CN (left) and CD_2Cl_2 (right), measured under identical conditions of concentration (7.33 mM) and temperature (25 °C). The large negative peak represents the spin-inverted proton signal, while the presence of positive peaks represents through-space communication with the spin-inverted proton. The asterisk on the NMR spectrum shown in right panel represents the solvent peak. See main text and the SI for additional details.

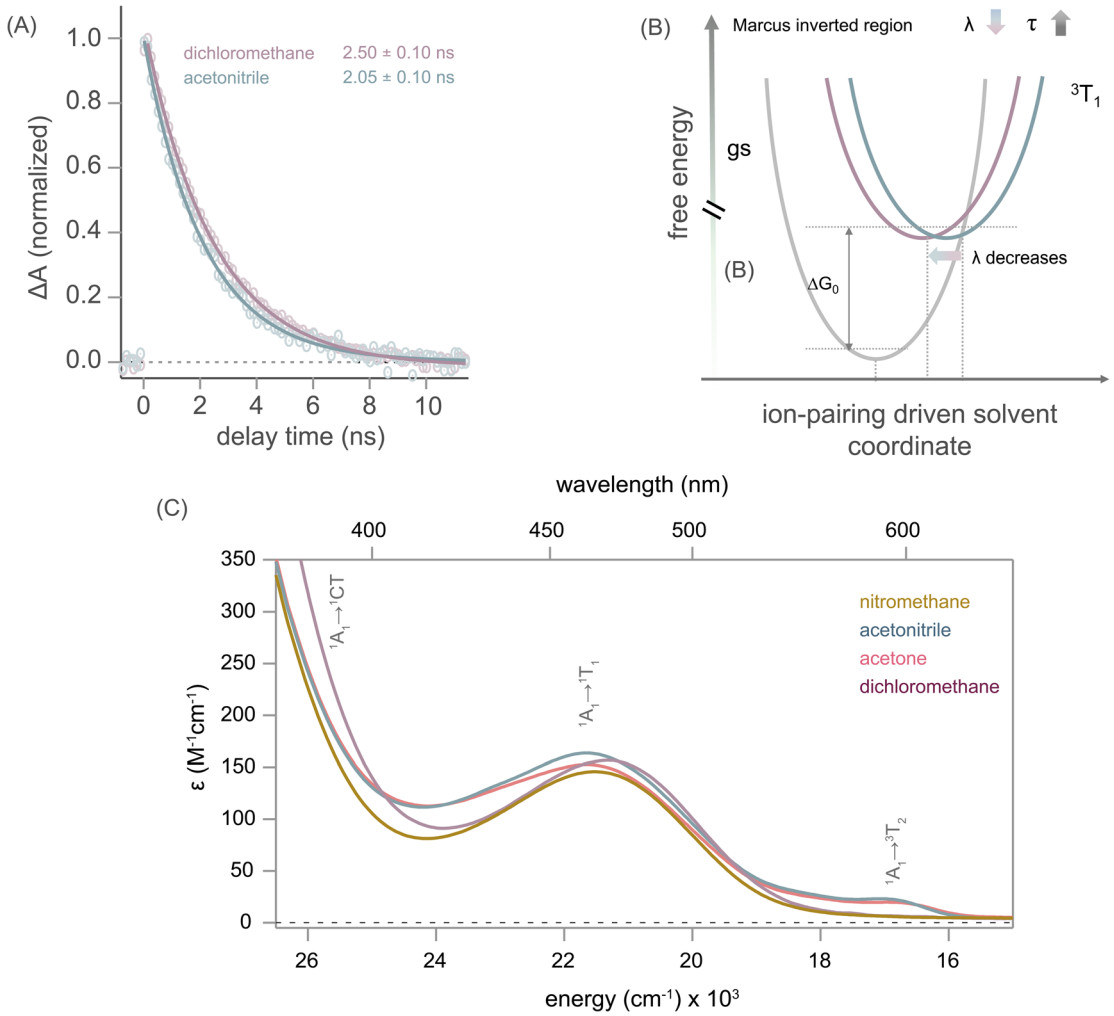

Fig. 5 (A) Time-resolved differential absorption data for $[Co(4,4'\text{-}OMebpy)_3](BAr^F{}_4)_3$ at 620 nm in room-temperature solutions of CH_2Cl_2 and CH_3CN following $^{1}A_1 \rightarrow {}^{1}T_1$ excitation at 480 nm. The solid lines correspond to fits of the data to single-exponential kinetic models. (B) Schematic representation of the potential energy surface diagram describing the effect of solvent reorganization on ground-state recovery dynamics. (C) Ground-state electronic absorption spectra of $[Co(4,4'\text{-}OMebpy)_3](BAr^F{}_4)_3$ in the four different solvents used in this study. See text for further details.

Ligand-field excited-state dynamics

With the degree and nature of ion-pairing in these various solvents now delineated, we turned our attention to the photophysical properties of the compound. We have previously shown that, following photoexcitation into the lowest energy spin-allowed ligand-field transition ($^1A_1 \rightarrow {}^1T_1$), compounds of this class undergo an ultrafast intersystem crossing to the lowest energy $^3T_1$ ligand-field excited state, followed by ground-state recovery ($^3T_1 \rightarrow {}^1A_1$) that occurs in the Marcus inverted region.[40,44] In the present study, $[Co(4,4'\text{-OMebpy})_3]^{3+}$ was photoexcited at 480 nm and monitored at 620 nm to quantify the time-scale for relaxation from the $^3T_1$ state back to the compound's ground state (Fig. 5A) in the four solvents used in the ion-pairing studies. The data were all well described by single-exponential kinetic models, the parameters for which are summarized in Table 2 for each solvent studied. As evident from the table, no systematic trend could be identified between the ground-state recovery lifetimes and the static dielectric constants of the solvents. This was not surprising given our previous work examining the solvent dependence of the ground-state recovery dynamics of $[Fe(bpy)_3]^{2+}$, where no clear correlation between excited-state lifetime and bulk solvent properties was readily identified.[54] That stated, we note that for the present study, the excited state lifetime in CH_2Cl_2 found to be longer than what was observed in the other three solvents. The compound in this solvent also exhibited the greatest degree of ion pairing.

To understand this observation, we examined these results in the context of non-radiative decay theory. While both Arrhenius and Transition state theory (*i.e.*, the Eyring equation) have been employed previously to understand dynamics of non-radiative decay processes within ligand-field manifolds,[44,55] semi-classical Marcus theory – which can be derived from generalized non-radiative decay theory by treating the nuclear part of the system classically – provides a convenient framework in the present case due to its explicit parameterization of reorganization energy. The expression for semi-classical Marcus theory is given in eqn (4),

$$k_{nr} = \frac{2\pi}{\hbar}|H_{ab}|^2 \frac{1}{\sqrt{4\pi\lambda k_B T}} \exp\left\{-\frac{(\Delta G_0 + \lambda)^2}{4\lambda k_B T}\right\} \quad (4)$$

where k_{nr} is the nonradiative decay constant (*i.e.*, the rate constant for ground-state recovery), ΔG_0 is the driving force (*i.e.*, the zero-point energy difference between the ground and excited states), H_{ab} represents the electronic coupling between the ground- and lowest-energy excited states, k_B and T are the Boltzmann constant and absolute temperature, respectively, and λ is the total reorganization energy comprised of both inner-sphere (λ_i) and outer-sphere (λ_o, *e.g.*, solvent) contributions. Solvent effects on ligand-field dynamics of d^6-complexes – specifically Fe(II) – have been the subject of previous studies,[54] however, to our knowledge the impact of ion-pairing on these processes has not been explored.

Although ligand-field transitions are largely insulated from solvent effects due to their localization on the metal centre,[56] we nevertheless considered any impact changes in the solvent might have on both the absorptive and lowest-energy excited state energies of the chromophore. The ground-state electronic absorption spectrum of $[Co(4,4'\text{-OMebpy})_3](BAr^F{}_4)_3$ in all four solvents are plotted in Fig. 5C and summarized in Table 2. As expected, the observed transition energies are relatively insensitive to changes in the solvent. These conclusions are supported by time-dependent DFT calculations. The details of these calculations can be found in the experimental methods section, but briefly, the ground state of $[Co(4,4'\text{-OMebpy})_3]^{3+}$ was optimized in all four solvents using previously reported methods,[44] followed by frequency calculations to confirm that the final structure corresponded to a minimum on the potential energy surface. Single-point energy calculations for the $^1T_1$ and $^3T_1$ ligand-field excited states were performed using the ground state geometry to obtain vertical transition energies, whereas the energy of the fully relaxed $^3T_1$ state was used to assess its zero-point energy relative to the ground state. Spin-allowed singlet excited state and spin forbidden triplet computed transition energies were found to match exceptionally well with the experimentally observed $^1A_1 \rightarrow {}^1T_1$ and $^1A_1 \rightarrow {}^3T_1$ energies, respectively.

This point notwithstanding, analysis of the three experimentally observed ligand-field transitions does indicate a small (<300 cm^{-1}) variation in the ligand-field splitting parameter (10Dq) as a function of solvent (Table S1). Focusing on the two extremes (*i.e.*, CH_3NO_2 and CH_2Cl_2), these data taken in isolation would predict a reduction in the excited-state lifetime of $[Co(4,4'\text{-OMebpy})_3]^{3+}$ in CH_2Cl_2 relative to CH_3NO_2 due to the inverted nature of the photophysics of this compound.[44] This prediction opposes the experimental result (Table 2), a fact that we believe rules out these small variations in the ground-state/excited-state zero-point energy difference as the origin of the observed change in lifetime. These considerations also apply to

Table 2 Experimental and DFT-estimated ligand field-state energies of $[Co(4,4'\text{-OMebpy})_3](BAr^F)_3$ in CH_3NO_2, CH_3CN, $(CH_3)_2CO$, and CH_2Cl_2 solutions, along with the experimentally measured ground-state recovery time constant determined by time-resolved absorption measurements following $^1A_1 \rightarrow {}^1T_1$ excitation in room-temperature solution

Solvents	Nitromethane	Acetonitrile	Acetone	Dichloromethane
$^1A_1 \rightarrow {}^1T_1$ (cm^{-1}),[a] (DFT)	21 600 (21 240)	21 690 (21 240)	21 720 (21 230)	21 420 (21 190)
$-\Delta G_0$ ($^3T_1$) (cm^{-1})[b]	10 500	10 500	10 495	10 470
GSR lifetime (ns)	2.30 ± 0.10	2.05 ± 0.10	2.05 ± 0.10	2.50 ± 0.10

[a] Energy at λ_{max} for the lowest-energy spin-allowed ligand-field transition (Fig. 5C, SI). [b] Calculated zero-point energy for the lowest-energy ligand-field excited state.

the influence of electronic coupling, wherein a decrease in the zero-point energy difference would lead to an increase in the magnitude of H_{ab} and concomitant decrease in the time constant for ground-state recovery. Since the experimental data trends in the opposite direction, we assert that the observed changes in excited-state lifetime are likewise not linked to this parameter in any straightforward manner. This leaves changes in the reorganization energy as the simplest, most likely origin of our observations.

As indicated above, the reorganization energy has two components, namely inner-sphere (λ_i) and outer-sphere (λ_o). Inner-sphere contributions are associated with the reactant(s) themselves: in the present case, λ_i will reflect the change in equilibrium geometries between the $^3T_1$ excited state and the $^1A_1$ ground state. While there are significant differences in structure between these two states (*e.g.*, the Jahn–Teller distortion associated with the $^3T_1$), we consider it unlikely that these intramolecular geometric changes will be solvent-dependent (a conclusion that is strongly supported by the TD-DFT calculations described previously).

Determining a microscopic origin for changes in outer-sphere reorganization energy is a challenging task. That stated, our knowledge about the intrinsic photophysics of this class of chromophores coupled with the information now afforded us concerning ion-pairing allows us to speculate as to the origin of these observations. Since the ground-state recovery dynamics for $[Co(4,4'\text{-OMebpy})_3]^{3+}$ occur in the Marcus inverted region, an increase in lifetime implies a decrease in reorganization energy at constant driving force (Fig. 5B). More specifically, the time-resolved data on $[Co(4,4'\text{-OMebpy})_3]^{3+}$ suggests a reduction in the magnitude of λ_o in CH_2Cl_2 relative to the higher dielectric constant solvents studied. Previous work from our group examined the influence of solvent on the excited-state relaxation dynamics of $[Fe(bpy)_3]^{2+}$.[54] As mentioned above, no simple correlation to any bulk solvent properties was evident, but correlations were found within families of solvents (*e.g.*, nitriles *vs.* alcohols *vs.* diols, *etc.*). This observation led to the conclusion that the volume contraction associated with conversion from the high-spin $^5T_2$ excited state of that compound to its low-spin $^1A_1$ ground state gave rise to an outer sphere contribution to the overall reorganization energy as the solvent responded to the concomitant increase in the charge density of the chromophore. The degree of contraction associated with ground-state recovery for $[Co(4,4'\text{-OMebpy})_3]^{3+}$ will be less than that of $[Fe(bpy)_3]^{2+}$ owing to the difference in the electronic structures of the excited states (*i.e.*, $(t_{2g})^4(e_g^*)^2$ for the $^5T_2$ state of Fe(II) *versus* $(t_{2g})^5(e_g^*)^1$ for the $^3T_1$ of Co(III)), but a phenomenologically similar effect is to be expected. In this regard, we note that CH_2Cl_2 happens to be the solvent not only with the most extensive degree of ion-pairing, but also, the only solvent of the four we examined for which contact ion pairs are the dominant species present at room temperature. In this circumstance, solvent will be largely excluded from the immediate vicinity of the cation due to the local proximity of the counterion. The dynamics associated with ground-state recovery would therefore occur in the absence of significant interactions with the solvent, which should in turn attenuate the degree to which the solvent would need to respond to accommodate the change in charge density of the cation. In the Marcus inverted region, this reduction in the magnitude of λ_o will result in more nested potentials and a decrease in the rate constant for excited-state decay (Fig. 5B). While additional, more subtle contributions may be at play – processes that would require a detailed, microscopic assessment of solvent–solvent and solvent-solute interactions[35] – we suggest that this attenuation in outer-sphere reorganization energy is the primary influence of ion-pairing on the excited-state dynamics of $[Co(4,4'\text{-OMebpy})_3]^{3+}$.

Conclusions

We have designed and synthesized a cobalt(III) polypyridyl complex as a model system to probe the extent of ion-pairing in non-aqueous solution using a combination of NMR spectroscopic methods. Variable-temperature DOSY measurements coupled with 1-D ROE experiments across four different solvents of varying dielectric strength provided unprecedented insights into the extent and nature of ion-pairing present in solution. Extensive ion-pairing was found in all the solvents as evidenced by diffusion constants measured for both the $[Co(4,4'\text{-OMebpy})_3]^{3+}$ cation and the $BAr^F{}_4^-$ anion: when combined with the results of 1D ROE measurements, our analyses allowed for a differentiation between solvent-separated and contact ion-pairs, an insight which proved essential in understanding changes in the photophysics of the compound. Ground-state recovery kinetics corresponding to $^3T_1 \rightarrow {}^1A_1$ ligand-field relaxation were collected across all four solvents using ultrafast time-resolved absorption spectroscopy, which were analysed through the lens of semi-classical Marcus theory. Supported by DFT and TD-DFT calculations and previous work on the intrinsic photophysics of this class of compounds, we suggest that ion-pairing leads to an attenuation of outer-sphere contributions to the total reorganization energy and is largely responsible for the observed increase in excited-state lifetime under conditions for which contact ion pairs are the dominant species present. We believe this study has demonstrated a reliable NMR-based methodology to probe ion-pairing in non-aqueous media, which in turn allows for an examination of its effect on the photophysical properties of metal complexes. Given the expanding interest in the use of earth-abundant compounds in a variety of contexts, we suggest that the ability to quantify ion-pairing and its influence on excited-state properties may provide researchers with a new tool for tailoring the photofunctionality of this class of chromophores.

Author contributions

A. G. conceived the central project idea and synthesized the complex. A. G. and D. H. designed and performed the NMR experiments. A. G. performed the transient absorption studies, analysed all data and prepared the figures for the manuscript. J. K. M. provided guidance throughout the project. All author contributed to preparing the manuscript.

Conflicts of interest

There are no conflicts to declare.

Data availability

All data supporting this article have been included either in the main manuscript or as part of the Supplementary Information.

Synthesis, characterization, additional NMR experiments, ligand-field absorption studies, computational details, transient absorption experiments. See DOI: **https://doi.org/10.1039/d5sc03015c**.

Acknowledgements

A. G. thank Björn Pfund for helpful comments on the initial draft of the manuscript. This work was supported in part through computational resources and services provided by the Institute for Cyber-Enabled Research at Michigan State University. The research was generously supported through the Chemical Sciences, Geosciences, and Biosciences Division, Office of Basic Energy Sciences, Office of Science, US Department of Energy under grant no. DE-FG02-01ER15282 and also through BioLEC (Bioinspired Light-Escalated Chemistry), an Energy Frontier Research Centre funded by the Office of Basic Energy Sciences, Office of Science, U.S. Department of Energy, under Award Number DE-SC0019370.

Notes and references

1 C. K. Prier, D. A. Rankic and D. W. C. MacMillan, *Chem. Rev.*, 2013, **113**, 5322–5363.
2 F. Glaser and O. S. Wenger, *Coord. Chem. Rev.*, 2020, **405**, 213129.
3 D. M. Arias-Rotondo and J. K. McCusker, *Chem. Soc. Rev.*, 2016, **45**, 5803–5820.
4 G. Morselli, C. Reber and O. S. Wenger, *J. Am. Chem. Soc.*, 2025, **147**, 11608–11624.
5 C. Förster and K. Heinze, *Chem. Phys. Rev.*, 2022, **3**, 041302.
6 A. Y. Chan, I. B. Perry, N. B. Bissonnette, B. F. Buksh, G. A. Edwards, L. I. Frye, O. L. Garry, M. N. Lavagnino, B. X. Li, Y. Liang, E. Mao, A. Millet, J. V. Oakley, N. L. Reed, H. A. Sakai, C. P. Seath and D. W. C. MacMillan, *Chem. Rev.*, 2022, **122**, 1485–1542.
7 K. Brak and E. N. Jacobsen, *Angew. Chem., Int. Ed.*, 2013, **52**, 534–561.
8 T. E. Schirmer and B. König, *J. Am. Chem. Soc.*, 2022, **144**, 19207–19218.
9 H. K. Adams, M. Kadarauch, N. J. Hodson, A. R. Lit and R. J. Phipps, *Chem. Rev.*, 2025, **125**(5), 2846–2907.
10 P. Li, C. Bourgois, F. Glaser, S. De Kreijger, A. Cadranel, L. Troian-Gautier and K. Hu, *J. Am. Chem. Soc.*, 2025, **147**(14), 12082–12091.
11 M. Schmitz, M. S. Bertrams, A. C. Sell, F. Glaser and C. Kerzig, *J. Am. Chem. Soc.*, 2024, **146**(37), 25799–25812.
12 Z. Qilei and D. G. Nocera, *Chem*, 2022, **8**, 1796–1799.
13 J. L. Ratkovec, J. D. Earley, M. Kudisch, W. P. Kopcha, E. Y. Xu, R. R. Knowles, G. Rumbles and O. G. Reid, *J. Phys. Chem. B*, 2025, **129**, 3895–3901.
14 Y. Marcus and G. Hefter, *Chem. Rev.*, 2006, **106**, 4585–4621.
15 A. Macchioni, *Chem. Rev.*, 2005, **105**(6), 2039–2074.
16 X.-X. Chen, X. Chen, F. Lan, T. Zeng, H. Cui and X. Zhang, *Org. Chem. Front.*, 2025, **12**, 3018–3027.
17 J. D. Earley, A. Zieleniewska, H. H. Ripberger, N. Y. Shin, M. S. Lazorski, Z. J. Mast, H. J. Sayre, J. K. McCusker, G. D. Scholes, R. R. Knowles, O. G. Reid and G. Rumbles, *Nat. Chem.*, 2022, **14**, 746–753.
18 Z. Xie, B. Cao, J. Zhao, M. Liu, Y. Lao, H. Luo, Z. Zhong, X. Xiong, W. Wei and T. Zou, *J. Am. Chem. Soc.*, 2024, **146**, 8547–8556.
19 W. J. Geary, *Coord. Chem. Rev.*, 1971, **7**, 81–122.
20 W. J. Vining, J. V Caspar and T. J. Meyer, *J. Phys. Chem.*, 1985, **89**, 1095–1099.
21 L. Wittenkeller, W. Lin, C. Diven, A. Ciaccia, F. Wang and D. M. De Freitas, *Inorg. Chem.*, 2001, **40**, 1654–1662.
22 N. F. A. Van Der Vegt, K. Haldrup, S. Roke, J. Zheng, M. Lund and H. J. Bakker, *Chem. Rev.*, 2016, **116**(13), 7626–7641.
23 G. Li, W. B. Swords and G. J. Meyer, *J. Am. Chem. Soc.*, 2017, **139**, 14983–14991.
24 W. B. Swords, G. Li and G. J. Meyer, *Inorg. Chem.*, 2015, **54**, 4512–4519.
25 W. B. Swords, G. J. Meyer and L. Hammarström, *Chem. Sci.*, 2020, **11**, 3460–3473.
26 W. M. Ward, B. H. Farnum, M. Siegler and G. J. Meyer, *J. Phys. Chem. A*, 2013, **117**, 8883–8894.
27 L. Troian-Gautier, E. E. Beauvilliers, W. B. Swords and G. J. Meyer, *J. Am. Chem. Soc.*, 2016, **138**, 16815–16826.
28 S. Ilic, D. R. Cairnie, C. M. Bridgewater and A. J. Morris, *J. Photochem. Photobiol.*, 2021, **8**, 100084.
29 J. Zanzi, Z. Pastorel, C. Duhayon, E. Lognon, C. Coudret, A. Monari, I. M. Dixon, Y. Canac, M. Smietana and O. Baslé, *JACS Au*, 2024, **4**(8), 3049–3057.
30 E. P. Farney, S. J. Chapman, W. B. Swords, M. D. Torelli, R. J. Hamers and T. P. Yoon, *J. Am. Chem. Soc.*, 2019, **141**, 6385–6391.
31 S. De Kreijger, M. Gillard, B. Elias and L. Troian-Gautier, *ChemCatChem*, 2024, **16**, e202301100.
32 M. J. Goodwin, J. C. Dickenson, A. Ripak, A. M. Deetz, J. S. McCarthy, G. J. Meyer and L. Troian-Gautier, *Chem. Rev.*, 2024, **124**(11), 7379–7464.
33 G. J. Kavarnos and N. J. Turro, *Chem. Rev.*, 1986, **86**(2), 401–449.
34 N. R. East, R. Naumann, C. Förster, C. Ramanan, G. Diezemann and K. Heinze, *Nat. Chem.*, 2024, **16**, 827–834.
35 M. Opperman, F. Zinna, J. Lacour and M. Chergui, *Nat. Chem.*, 2022, **14**, 739–745.
36 T. H. Bürgin, F. Glaser and O. S. Wenger, *J. Am. Chem. Soc.*, 2022, **144**, 14181–14194.
37 P. S. Wagenknecht and P. C. Ford, *Coord. Chem. Rev.*, 2011, **255**, 591–616.
38 C. Wegeberg and O. S. Wenger, *JACS Au*, 2021, **1**, 1860–1876.
39 K. Behm and R. D. McIntosh, *ChemPlusChem*, 2020, **85**, 2611–2618.

40 A. Y. Chan, A. Ghosh, J. T. Yarranton, J. Twilton, J. Jin, D. M. Arias-Rotondo, H. A. Sakai, J. K. McCusker and D. W. C. MacMillan, *Science*, 2023, **382**, 191–197.
41 M. M. Alowakennu, A. Ghosh and J. K. McCusker, *J. Am. Chem. Soc.*, 2023, **145**, 20786–20791.
42 S. I. Ting, S. Garakyaraghi, C. M. Taliaferro, B. J. Shields, G. D. Scholes, F. N. Castellano and A. G. Doyle, *J. Am. Chem. Soc.*, 2020, **142**(12), 5800–5810.
43 P. Yaltseva and O. S. Wenger, *Science*, 2023, **382**, 153–154.
44 A. Ghosh, J. T. Yarranton and J. K. McCusker, *Nat. Chem.*, 2024, **16**, 1665–1672.
45 J. T. Yarranton and J. K. McCusker, *J. Am. Chem. Soc.*, 2022, **144**, 12488–12500.
46 L. L. Jamula, A. M. Brown, D. Guo and J. K. McCusker, *Inorg. Chem.*, 2014, **53**, 15–17.
47 M. J. Frisch, G. W. Trucks, H. B. Schlegel, G. E. Scuseria, M. a. Robb, J. R. Cheeseman, G. Scalmani, V. Barone, G. a. Petersson, H. Nakatsuji, X. Li, M. Caricato, a. V. Marenich, J. Bloino, B. G. Janesko, R. Gomperts, B. Mennucci, H. P. Hratchian, J. V. Ortiz, a. F. Izmaylov, J. L. Sonnenberg, Williams, F. Ding, F. Lipparini, F. Egidi, J. Goings, B. Peng, A. Petrone, T. Henderson, D. Ranasinghe, V. G. Zakrzewski, J. Gao, N. Rega, G. Zheng, W. Liang, M. Hada, M. Ehara, K. Toyota, R. Fukuda, J. Hasegawa, M. Ishida, T. Nakajima, Y. Honda, O. Kitao, H. Nakai, T. Vreven, K. Throssell, J. a. Montgomery Jr, J. E. Peralta, F. Ogliaro, M. J. Bearpark, J. J. Heyd, E. N. Brothers, K. N. Kudin, V. N. Staroverov, T. a. Keith, R. Kobayashi, J. Normand, K. Raghavachari, a. P. Rendell, J. C. Burant, S. S. Iyengar, J. Tomasi, M. Cossi, J. M. Millam, M. Klene, C. Adamo, R. Cammi, J. W. Ochterski, R. L. Martin, K. Morokuma, O. Farkas, J. B. Foresman and D. J. Fox, *Gaussian 16, Revision C.01*, Gaussian, Inc., Wallin, 2016.
48 C. Kreitner, A. K. C. Mengel, T. K. Lee, W. Cho, K. Char, Y. S. Kang and K. Heinze, *Chem.–Eur. J.*, 2016, **22**, 8915–8928.
49 E. J. Cabrita and S. Berger, *Magn. Reson. Chem.*, 2001, **39**, S142–S148.
50 A. W. J. Poh, J. A. Aguilar, A. M. Kenwright, K. Mason and D. Parker, *Chem.–Eur. J.*, 2018, **24**, 16170–16175.
51 P. S. Pregosin, *Prog. Nucl. Magn. Reson. Spectrosc.*, 2006, **49**, 261–288.
52 K. E. Aldrich, B. S. Billow, D. Holmes, R. D. Bemowski and A. L. Odom, *Organometallics*, 2017, **36**, 1227–1237.
53 C. J. Seeton, *Tribol. Lett.*, 2006, **22**, 67–78.
54 J. N. Miller and J. K. McCusker, *Chem. Sci.*, 2020, **11**, 5191–5204.
55 M. C. Carey, S. L. Adelman and J. K. McCusker, *Chem. Sci.*, 2019, **10**, 134–144.
56 H. Aust and G. Lehmann, *J. Solution Chem.*, 1977, **6**, 443–453.